The Seasat Scanning Multichannel Microwave Radiometer (SMMR): Instrument Description and Performance

ENI G. NJOKU, MEMBER, IEEE, J. M. STACEY, AND FRANK T. BARATH

Abstract—The scanning multichannel microwave radiometer (SMMR) is an imaging 5–frequency radiometer flown on the Seasat and Nimbus-7 earth satellites launched in 1978. It measures dual-polarized microwave radiances from the earth's atmosphere and surface, primarily for the purpose of deriving global and nearly all-weather measurements of sea surface temperature, wind speed, and atmospheric liquid water and water vapor. This paper describes the SMMR instrument and its calibration, antenna pattern measurements, and data processing procedures. Analysis of early data from the Seasat SMMR shows that the expected engineering performance in flight was achieved, and the measurement of sea surface temperature and wind speed with accuracies of 1.5 K and 2 m/s, respectively, may be achievable once the geophysical data processing algorithms and analysis have been completed.

I. INTRODUCTION

THE SCANNING multichannel microwave radiometer (SMMR), designed to be flown on the Seasat and Nimbus-7 earth satellites, is a 5-frequency imaging microwave radiometer. It measures dual-polarized microwave radiation from the earth's atmosphere and surface at frequencies of 6.63, 10.69, 18.0, 21.0, and 37.0 GHz. A variety of geophysical parameters can be derived from these 10 channels of data, as demonstrated through laboratory, aircraft, balloon, and spacecraft experiments carried out since the early 1960's [1]–[9]. The microwave measurements of the earth's surface have the advantage that they are relatively insensitive to cloud cover and can be made under nearly all-weather conditions. Specifically, the SMMR data can be analyzed to derive the following parameters: sea surface temperature, sea surface wind speed, atmospheric water vapor, cloud and precipitating liquid water, and sea ice age and coverage. Information on soil moisture and terrain snow cover properties and extent can also be obtained. The algorithms used to retrieve the geophysical parameters require accurately known brightness temperatures at the antenna collecting aperture at each frequency and polarization. These requirements, coupled with the need for high spatial resolution and wide swath, have combined to challenge the spaceborne radiometer technology state of the art in both the hardware and the calibration areas. This paper describes the design and calibration of the SMMR, its data processing including a brief description of the calibration and antenna pattern correction (APC) algorithms, and pre-

sents the in-flight performance and early science data from the instrument flown on the Seasat spacecraft. The calibration and APC algorithms are described in detail in the companion papers [10] and [11].

II. INSTRUMENT DESCRIPTION

A. Functional Requirements

The functional requirements for the SMMR instrument, initially developed for the same experiment on the Nimbus-7 spacecraft, are tabulated in Table I and have been discussed previously by Gloersen and Barath [12]. In addition to the items listed, it was specified that the antenna beams at the five frequencies should be coincident and that a swath width of 50° angular extent should be covered with a conical scan having a cone half-angle of 42° from the local vertical. These requirements were known to be difficult to achieve, particularly in the antenna area where in fact some of the specifications had to be relaxed during the implementation phase of the project.

B. General Description

A front view of the SMMR instrument in its handling fixture is shown in Fig. 1. The instrument weighs 55 kg which includes 25 kg for the antenna and scan machanism, and its operating power requirement is 65 W. The instrument consists of six independent and identical Dicke-type superheterodyne radiometers fed by an antenna and a calibration subsystem, delivering smoothed analog output signals to a data multiplexer-programmer. The information is encoded together with auxiliary information, and then sent to the spacecraft data system for transmission to earth. Fig. 2 shows the system block diagram: at 37 GHz two radiometers simultaneously measure the horizontal and vertical components of the received signal; at the other four frequencies, the radiometers alternate between the two polarizations during successive scans. In this manner, ten data channels corresponding to five dual-polarized signals are provided by the instrument.

The instrument possesses a scanning antenna system which consists of an offset parabolic reflector with a 79-cm diameter collecting aperture and a multifrequency feed assembly. The antenna reflector is mechanically scanned with a sinusoidally varying velocity, over a 50° swath angle, and with a 4-s time period. The antenna beams produce contiguous footprints on the surface in the pattern shown in Fig. 3. The pattern is offset 22° from the subsatellite track to permit better coincidence with the coverage pattern of the other Seasat sensors.

TABLE I
SMMR FUNCTIONAL REQUIREMENTS

	6.633	10.69	18	21	37
Frequency, GHz	6.633	10.69	18	21	37
Tolerance (1σ), MHz	5	8	14	16	28
Wavelength, cm	4.52	2.81	1.67	1.43	0.81
Polarization	Vert & Horiz	Vert & Horiz	Vert & Horiz	Vert & Horiz	Vert & Horiz
Antenna 3dB Beamwidth, deg	4.2	2.6	1.6	1.4	0.8
Tolerance (1σ)	0.2	0.15	0.1	0.1	0.1
Polarization Isolation, dB	>25				
Pointing Accuracy, deg (1σ)	0.1				
Solid Angle Beam Efficiency*, %	87				
Integration Time, ms	126	62	62	62	30
Temperature Resolution, K(1σ) (300 K Target)	0.9	0.9	1.2	1.5	1.5
Absolute Temperature Accuracy, K (1σ)	2				
Dynamic Temperature Range, K	10 – 330				
Temperature Stability (24 Hours), K (1σ)	1				

*Beam efficiency is defined here as the ratio of the energy received within
2.5 x the half-power beamwidth at one polarization to the total energy
received, when the antenna is surrounded by an isothermal black body.
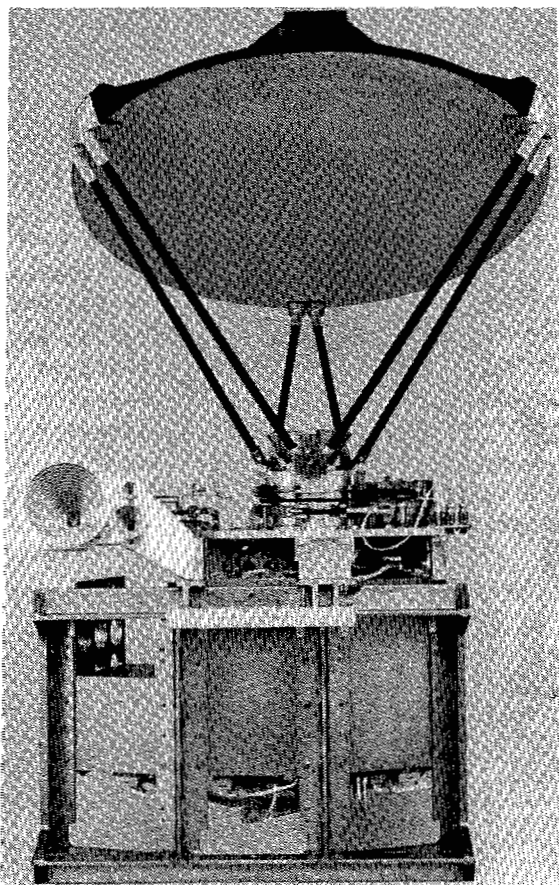

Fig. 1.   The SMMR instrument.

Calibration is obtained by alternately switching in a "cold horn" viewing deep space and a "calibration load" at ambient temperature at the scan extremes.

The ground support equipment for the instrument consists of a bench checkout equipment (BCE) facility and calibration equipment. The BCE performs two functions: it simulates the spacecraft by providing power and timing signals to the instrument, and it receives and records the output data. The built-in minicomputer allows limited real-time manipulation of the data for display and basic performance verification purposes. The calibration equipment allows the quantitative determination of the instrument characteristics at all levels, from individual components to the overall system. It includes standard laboratory test equipment, facilities such as antenna ranges and thermal-vacuum chambers, and an assortment of specially designed blackbody targets and calibration devices. Except for the blackbody targets which will be described in more detail in Section III, these facilities and equipment are straightforward in configuration and will not be discussed further.

C. Antenna and Scan Mechanism

The reflector is supported by a hexapod structure attached to a ring surrounding the feed horn. Both the reflector and the pods are made from graphite-epoxy; the reflector is aluminized and the pods are wrapped with aluminum foil for thermal and electrical reasons.

The multifrequency feed horn (MFFH) is a ring-loaded corrugated conical horn with a sequence of waveguide tapers,
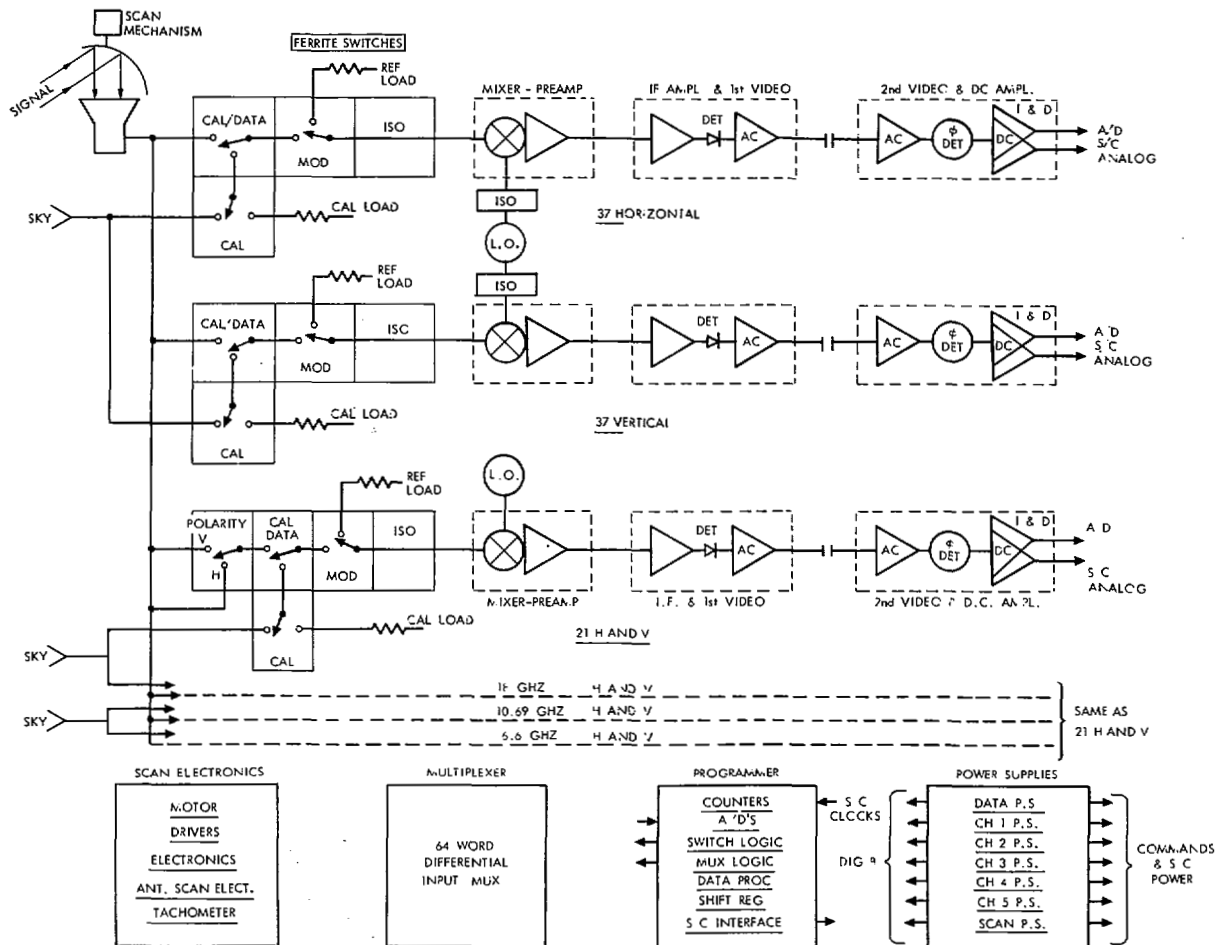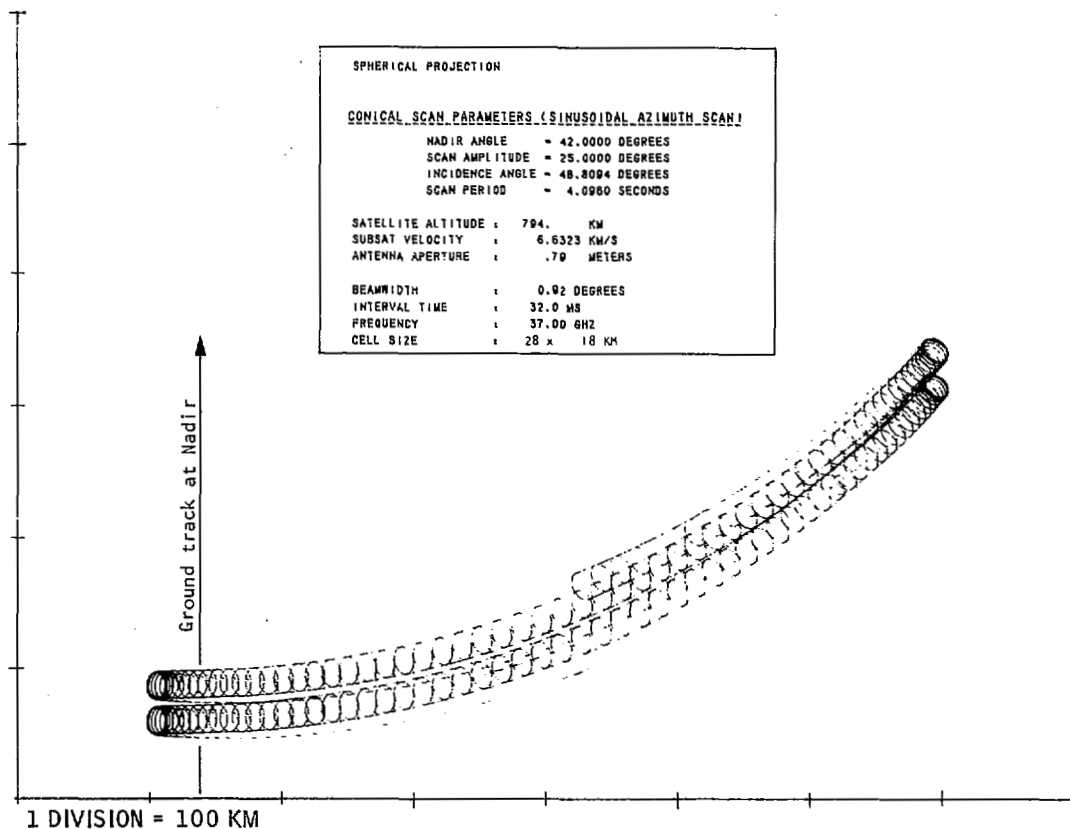
Fig. 2.   SMMR functional schematic diagram.

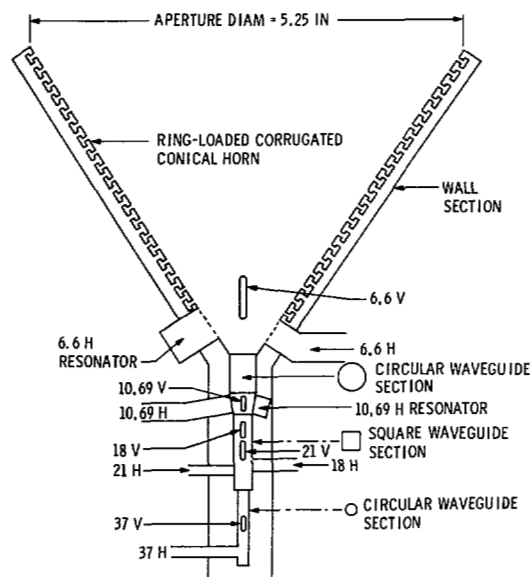Fig. 3.   Seasat SMMR scan pattern at 37 GHz.

Fig. 4.   SMMR MFFH.

TABLE II
SUMMARY OF SEASAT SMMR ANTENNA MEASUREMENTS

Frequency, GHz	Polarization	Half-Power Beamwidth, degrees	Beam Efficiency*, percent	Cross-Polarization Isolation[+], dB	Dissipative Feed Loss, dB
6.6	V	4.56	79.7	−21.5	0.55
6.6	H	4.51	83.4	−19.9	0.55
10.69	V	2.93	83.8	−16.6	0.35
10.69	H	2.91	86.2	−16.1	0.37
18	V	1.80	85.2	−21.2	0.50
18	H	1.81	88.7	−20.1	0.52
21	V	1.50	84.2	−19.5	1.03
21	H	1.49	85.8	−18.4	1.03
37	V	0.93	88.2	−17.9	0.7
37	H	0.93	90.0	−17.4	0.7

*Beam efficiency defined as in Table 1. (These beam efficiencies include both co- and cross-polarized power and are from 2 to 4% lower than efficiencies calculated by considering co-polarized power alone.)

[+]Integrated over main beam.

resonators, and orthomode transducers at the throat, as shown in Fig. 4. It has ten waveguide output ports corresponding to vertical and horizontal signals at five frequencies, and is made of aluminum. Table II summarizes the measured characteristics of the complete antenna. The antenna pattern measurements are discussed in Section IV. The cold calibration horns are similar in design to the feed horn; three scaled horns are provided to yield beamwidths of about 25° at all frequencies. The largest horn serves the 6.6- and 10.69-GHz channels, the middle horn the 18- and 21-GHz channels, and the smallest the 37-GHz channels.

The scan system consists of a scan mechanism and drive electronics. The mechanism is based on a 3-phase delta-connected brushless (electronically commutated) dc motor with 48 permanent magnet pole pairs and integral 1024-line optical tachometer. The motor is of inside-out construction, the rotor with the magnets being around the stator. The antenna hexapod supporting ring is driven back and forth by the friction-clutch equipped motor shaft through a double cogged belt. One end of the belt is attached to the ring, the other to an idler wheel. A separate belt off the antenna ring drives a dual (redundant) 12-bit optical shaft angle encoder for antenna position readout. The belts are of polyurethane impregnated Dacron-filament construction.

The hexapod support ring rides on three external *V*-grooved rollers, two of which are hard mounted and the third of which is flexible to provide radial loading. The motor rotor is supported by sealed bearings. Both the rotor and the ring are
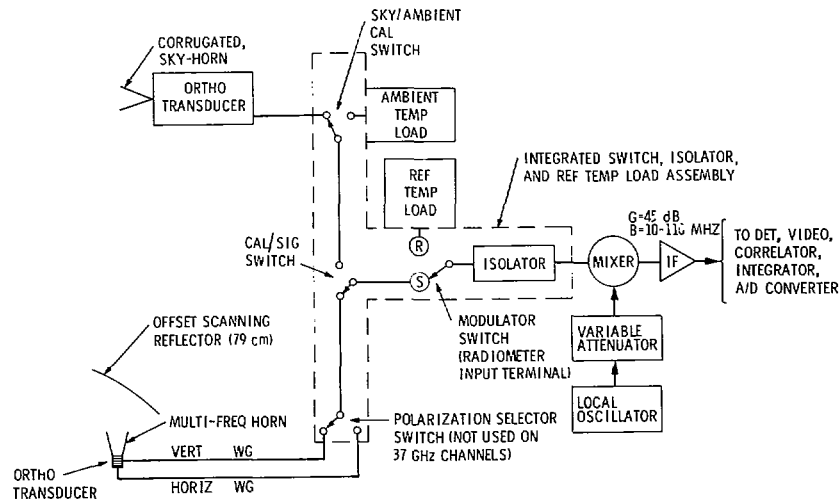
Fig. 5.   SMMR RF components.

caged during launch by V bands, each with two pyrotechnic piston motors (squibs), the firing of either of which will release the band. In the case of the antenna ring, the three roller bearings are spring loaded axially in such a manner that a 0.05-in separation between the ring and its clamping surface is effected upon band release. In the case of the motor, the rotor is made of flexure-connected outer and inner pieces and the outer piece is clamped down by the V band when caged.

Belting of the system is so arranged that the motor and the antenna are counter-rotating. Angular momentum compensation is accomplished by loading the motor rotor, which acts as a flywheel, with the proper mass. A residual momentum about the scan axis of less than 0.005 lb·ft·s peak when scanning was achieved in this manner. Static balancing is accomplished by adjustable tungsten weights on the antenna reflector.

The motor drive electronics consist of a second-order servo loop which uses rate feedback signals from the tachometer and position signals from the shaft angle encoder to drive the antenna reflector back and forth at a sinusoidally varying rate. A square wave input from the data-programmer unit provides synchronization with the rest of the instrument and the spacecraft. Commands are available from the spacecraft to power the scan system, to enable the scan, and to set the scan to zero (center of scan position). Either of the two shaft angle encoders can also be selected by command. In operation, the scan system attains steady-state scanning within 12 s (3 scan cycles) with a position error of less than 0.01 degree in amplitude with respect to a true sinusoid.

D. RF Assembly

A schematic diagram of the RF components for one typical radiometer channel is shown in Fig. 5. A modulator ("Dicke") switch alternates at approximately a 1-kHz rate between a reference temperature waveguide load and an input signal. This input can be either a vertical or horizontal polarized signal from the MFFH, or a calibration signal from either the sky horn or an ambient temperature load, as selected by the switches. These switches together with an isolator are
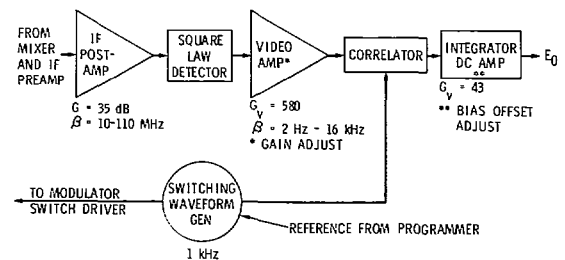

Fig. 6.   Typical SMMR electronics.

packaged into a single integrated unit for low loss and isothermal operation. The switches are latching ferrite circulators controlled by the programmer electronics. The mixer is a Schottky-barrier diode balanced double-sideband mixer with an integral IF preamplifier having a 10- to 110-MHz bandwidth. The local oscillator is a fundamental-frequency cavity-stabilized GaAs Gunn diode. As noted, all channels are identical except for the 37-GHz channels where there is no polarization selector switch.

E. Electronics Assembly

Fig. 6 shows the functional schematic of a typical set of electronics for each channel, with performance parameters indicated. The design is straightforward using integrated circuits and is of a type previously used on several spaceborne radiometers such as the Nimbus-5 NEMS and Nimbus-6 SCAMS instruments. The output of each channel is routed to the spacecraft backup data system and to the SMMR data-programmer unit.

The data-programmer unit in the electronics assembly provides the instrument timing, sequencing, multiplexing, and synchronizing signals. Included in this unit are a multiplexer for engineering and temperature monitoring, seven 12-bit A/D converters, shift registers, and timing circuits which interface with both the instrument and the spacecraft. Analog data from each of the channels are fed to individual A/D converters, and the A/D outputs are commutated in sequence into shift registers, then directed to the spacecraft data stream. A seventh A/D converter accepts multi-
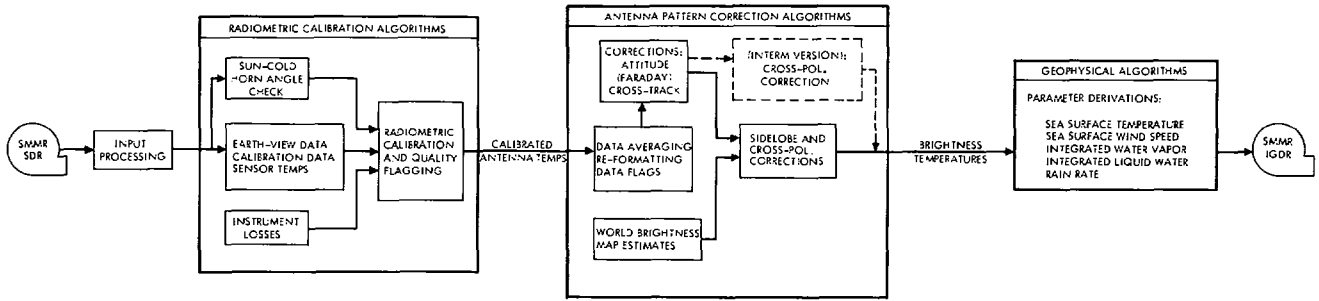
Fig. 7. SMMR data processing flow diagram.

plexed analog engineering signals from the instrument and delivers a digital stream to the spacecraft data system. The programmer also provides formatting and buffering functions between the instrument and the spacecraft digital systems.

The electronics for the antenna scan mechanism are also located in the electronics assembly. The operation of this module has been described in the paragraph dealing with the scan subsystem.

F. Power Supply Assembly

The power supply assembly consists of seven individual power supplies, each independently commandable on or off by the spacecraft command system. Each supply is energized from the −24.5-V spacecraft bus. One of six identical supplies provides for each radiometer channel 5 to 14 V from a high power switching regulator to the solid-state local oscillator, +15 and −15 V from low power switching regulators to the mixer-preamplifier and IF amplifier, +15 V from a low power switching regulator to the switch drive, and +15 V from a low power switching regulator to the video amplifier.

The seventh power supply energizes the data-programmer unit. It provides −15 V and +5 V from high power switching regulators. In addition, when this supply is turned on and the data-programmer unit comes up, a 20-kHz synchronization signal is fed to all of the power supplies. Normally, the data-programmer power supply will be turned on first in the operating sequence. If this procedure is not followed, the other power supplies will free-run at approximately 10.5 kHz, out of synchronism with the spacecraft clock. This type of operation will not endanger any portion of the instrument. However, none of the radiometer channels will operate unless the data-programmer power supply is on because the modulator switch drive (1 kHz) originates in this unit after being counted down from the spacecraft clock. In addition, the integrate and dump signals for each of the channels originate in the programmer.

An additional independent power supply located with the scan electronics energizes the scan subsystem. It provides +15 V and −15 V from high power switching regulators. This supply is also normally synchronized by the 20-kHz signal from the data-programmer unit.

G. Data Processing Flow

The SMMR data processing flow is illustrated schematically in Fig. 7 which shows the three functional stages in the data processing. The SMMR digital bit stream is extracted from the Seasat master sensor data record (MSDR) in the ground processing to form the SMMR sensor data record (SDR). The SDR contains all the SMMR radiometric and engineering data in addition to satellite and footprint location data. The SDR is the input to the data calibration stage of SMMR processing which converts digital radiometer output voltages to antenna temperatures. The antenna temperatures are then input to the APC algorithms which reformat the data, compensate for antenna sidelobe and polarization coupling effects, and perform a number of other minor operations such as Faraday rotation corrections (if necessary), attitude corrections, and sun location and data quality flagging. The brightness temperatures with grid locations in latitude and longitude and time tags are then passed on to the final stage of geophysical processing.

III. RADIOMETER CALIBRATION

In order to relate the radiometer output voltages to the input antenna temperatures of the SMMR operating on the spacecraft a calibration equation is used which makes use of data from the two calibration points. This calibration equation is obtained by applying radiative transfer to each of the lossy components between the antenna and the calibration switch output. The radiative transfer calibration equation can be reduced to the form

$$T_A = (a_0 + a_1 T_1 + a_2 T_2 + a_3 T_3 + a_6 T_i)$$
$$+ (a_4 T_4 + a_5 T_5 + a_7 T_i + a_8 T_s)(D_t - D_i)/(D_i - D_s)$$
$$+ a_9 (T_4 - T_s)^2 \{(D_t - D_i)/(D_i - D_s)\} \qquad (1)$$

in which a_0 through a_9 are lumped loss constants of the various waveguides and switches, T_1 through T_5 are the physical temperatures of the components as measured by attached platinum-resistance sensors, T_i is the ambient temperature of the calibration load, and T_s is the "cold space" temperature 2.7 K. The quantities D_t, D_i, and D_s are the counts measured by the radiometer when switched to the MFFH, the ambient load, and the sky horn, respectively, and T_A is the resulting calibrated antenna temperature. The values of the constants a_0 through a_9 are determined from laboratory measurements of the components and from radiometric measurements in the thermal-vacuum chamber. Equation (1) contains a quadratic term which accounts for the small (less than 1 percent) nonlinearity in the instrument. The derivation and analysis of (1) is described in [11].
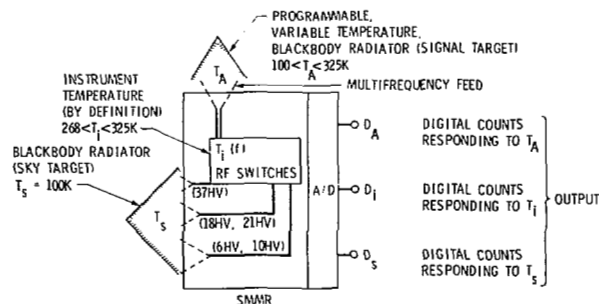
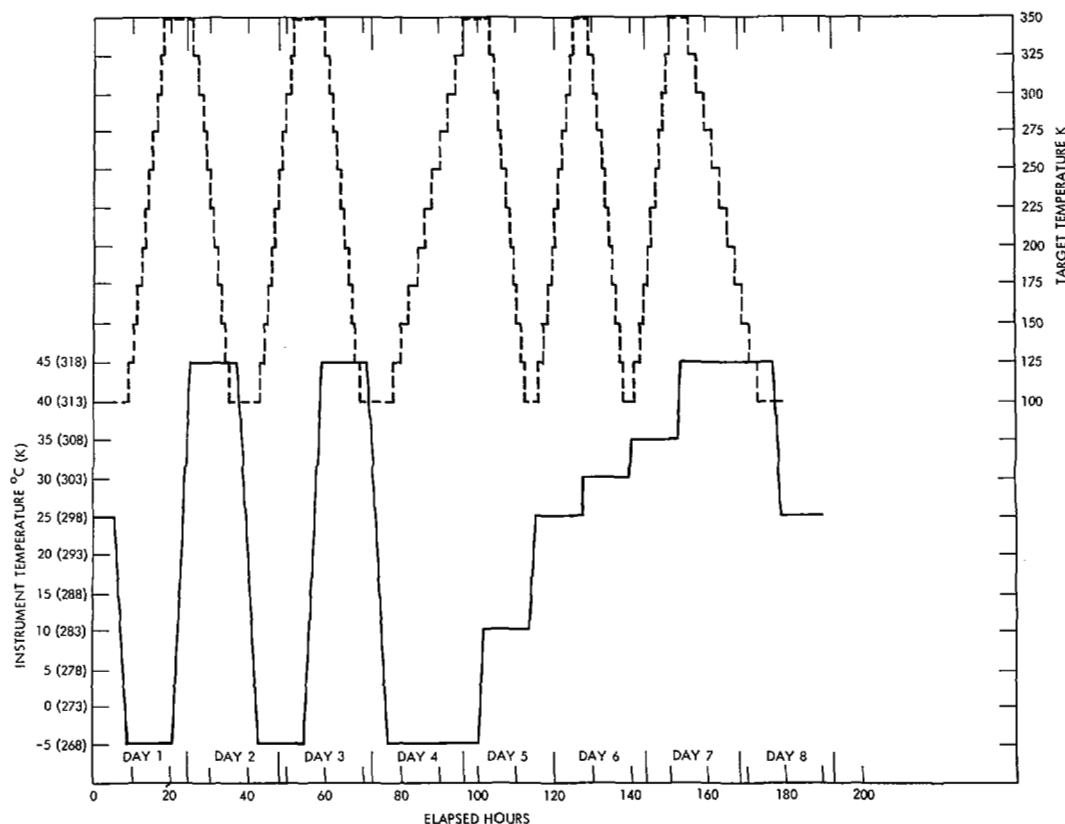Fig. 8.   SMMR thermal-vacuum environment instrument calibration.

Fig. 9.   SMMR temperature cycles in thermal vacuum.

The SMMR instrument is calibrated before launch in the thermal-vacuum chamber to simulate the environmental conditions to be experienced in space and to derive accurate values for the constants in the calibration (1). The calibration process is implemented in the thermal-vacuum chamber as shown in Fig. 8. The instrument is supported by a test fixture with cold-wall thermal radiators. Copper coils attached to the radiators circulate liquid and gaseous nitrogen to vary the instrument temperature over the range of temperature plateaus as shown in Fig. 9. The MFFH views a blackbody target (signal target) which is varied in temperature plateaus ranging from 100 to 350 K at each instrument temperature plateau. The target temperature is also controlled by circulating liquid and gaseous nitrogen through coils that are attached to the metal walls of the target that support the absorber material. The signal target configuration is a re-entrant pyramid with Brewster-angle absorption properties in the facets of the
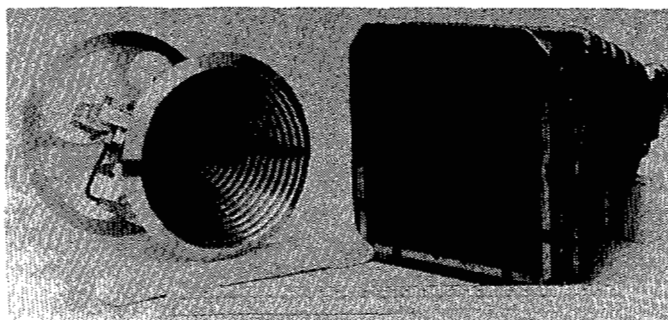

Fig. 10.   MFFH with signal calibration target.

absorber elements (see Fig. 10). The sky-calibration horns view simultaneously a similar blackbody target whose temperature is fixed at 100 ±2 K during the entire calibration process. The emissivity of the blackbody targets was estimated to be on the order of 0.999 at all frequencies and polarizations

as indicated by measured VSWR's of less than 1.05. Thus insignificant microwave temperature error is anticipated in assuming unit emissivity for the targets. The absorber is a ferrite-loaded epoxy material. The physical temperatures of the targets are monitored by multiple platinum-resistance sensors embedded within the absorber material. The instrument temperature is defined by the platinum-resistance sensor secured to the reference temperature load. The accuracy of the feeds are visible) to prevent nonuniform heating of the vacuum chamber, and in space, the entire instrument is shrouded in a thermal blanket (only the collecting apertures of feeds are visible) to prevent nonuniform heating of the instrument caused by the sun or other thermal radiations. One shortcoming of the calibration procedure is that the sky calibration target temperature of 100 K does not simulate the 2.7 K space temperature. Thus the modeled radiometer performance down to 2.7 K and the laboratory measured losses of the sky horn components are relied upon in using (1). For further discussion of the radiometer calibrations see [11].

IV. APC's

The calibration procedures described in the previous section relate the voltage outputs of the radiometers to the input antenna temperatures which are measures of the radiation intensity received by the antenna. The antenna receives radiation from all directions as weighted by the antenna patterns, and radiation received through the sidelobes and cross-polarization lobes must be corrected in order to derive the true brightness temperatures viewing in the direction of the antenna boresight. Procedures for making the APC's rely on having obtained accurate antenna pattern measurements over the entire 4π solid angle. These measurements were made prior to launch on the Jet Propulsion Laboratory (JPL) antenna range.

A. Antenna Pattern Measurements

The goal of the measurements on the antenna range was to acquire accurate and detailed antenna pattern measurements at each of the SMMR operating frequencies and polarizations. The measurements were conducted in the far field of the 79-cm aperture with the sky horns and thermal and RF shields simulated in place. Because of the antenna polarization rotation as a function of reflector scan position, and the additional variation in the effects of the back-up structure relative to the antenna boresight, small differences in the antenna patterns with changing scan position were expected. On one model of the SMMR, antenna patterns were measured at intervals of scan angle between $-25°$ and $+25°$ for the frequencies 6.6, 10.69, and 18 GHz. Results showed that the antenna pattern scan angle dependence is weak and approximately antisymmetric about a vertical plane through the antenna. Hence patterns made at $0°$ and $25°$ were considered adequate to characterize the variations with scan angle for all frequencies. Analysis of the antenna patterns did not show any significant effects of aperture blockage by the cold sky horns.

For each frequency, polarization, and scan angle, measurements of both the co- and cross-polarized patterns were made
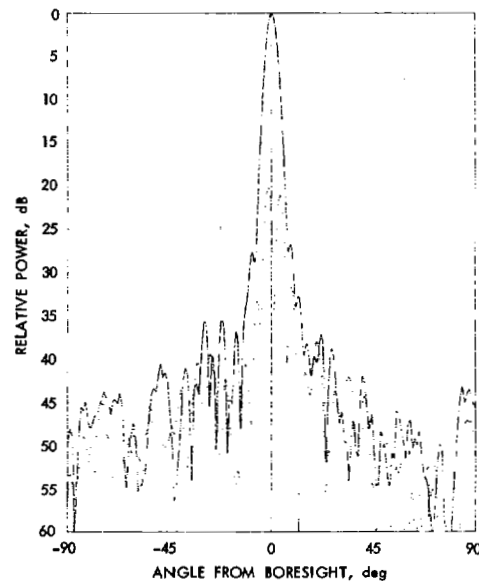

Fig. 11.   Seasat SMMR antenna patterns at 6.6-GHz horizontal polarization, $0°$ scan position, $0°$ cut angle (solid line is co-polarized, dotted is cross-polarized).

along planar cuts every $5°$ in azimuth about the boresight direction (over the range $\phi = 0°$ to $180°$), for a total of 36 cuts. Along each cut measurements were made over the range $\theta = -180°$ to $+180°$ to cover the entire solid angle. Since the greatest accuracy in the antenna patterns was required close to the antenna boresight, the measurements were made at the following increments of $\theta \mid \theta \mid = 0°$ (beamcenter) to $5°$ in increments of $0.02° \mid \theta \mid = 5°$ to $25°$ in increments of $0.5°$; and $\mid \theta \mid = 25°$ to $180°$ in increments of $1°$.

The 6.6-GHz horizontally polarized antenna patterns for the central scan position are shown for illustration in Figs. 11 and 12. Fig. 11 is a cut in the horizontal plane $\phi = 0°$, the solid line is the co-polarized pattern, and the dotted line is the cross-polarized pattern. Of interest is the existence of the two cross-polarization lobes about 20 dB down from the co-polarized main lobe, and the comparable sidelobe levels of the co- and cross-polarized patterns away from the boresight region. These features are characteristics of offset-fed parabolic reflector antennas [13]. Fig. 12 shows contour plots of the same antenna patterns. Azimuthal asymmetry in the co-polarized pattern is evident in Fig. 12(a) especially at levels of -15 dB and below, and is primarily due to the effects of the reflector support struts. These characteristics of the antenna patterns are important in the derivations of corrected brightness temperatures from the SMMR measurements.

The antenna patterns were integrated numerically to provide the beam efficiency and polarization isolation quantities given in Table II.

B. Corrections for Antenna Pattern Effects

As was mentioned previously the radiometric antenna temperature measurements require correction for effects introduced by the antenna patterns in order to obtain accurate
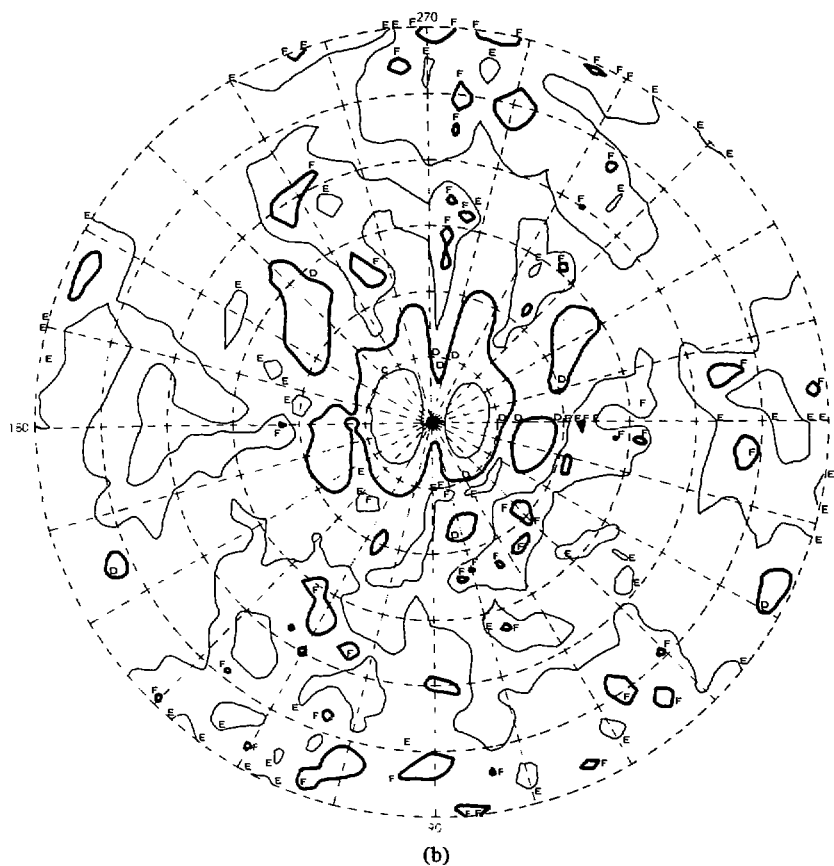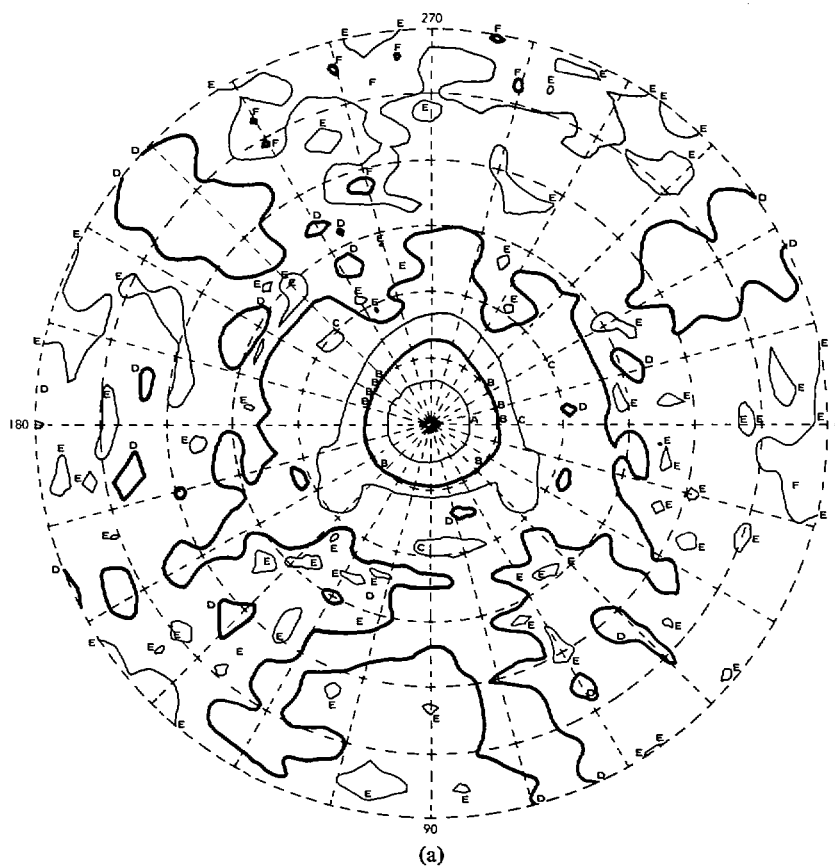
(a)

(b)

Fig. 12.   Seasat SMMR antenna pattern contour plots at 6.6-GHz horizontal polarization, 0° scan position. (a)Co-polarized.
(b) Cross polarized. (The outer limit of the plots is at | θ | = 30°; contour lines are at decreasing intervals of 10 dB as
follows: A = −5 dB, B = −15 dB, C = −25 dB, D = −35 dB, E = −45 dB, F = −55 dB.)

brightness temperatures. The SMMR APC accuracy requirements are more stringent than has been the case with previous sensors due to the goal of better than 1.5 K accuracy in obtaining sea surface temperatures. The main problem concerns making a correction for radiation received by the antenna through the sidelobes, so that the corrected value represents the average brightness temperature over the main-beam footprint region only. In some cases the beam efficiencies are 85 percent or less (Table II) and the corrections are quite large. Since the cross-polarized power in the main-beam is on the order of 20 dB below the co-polarized, a correction must be made also for the fact that on the order of 1-percent horizontally polarized radiation is being received in the vertical antenna port, and vice versa for the horizontal port. A much larger contribution to this polarization coupling arises from the fact that the antenna feed horn remains fixed as the reflector scans, resulting in a rotation of the effective antenna polarization vectors relative to the polarizations of the received surface radiation. Another effect which arises due to the integration times of the various radiometer channels and their different beamwidths is that the data values for the channels correspond to different locations sinusoidally spaced in the cross-track direction, and represent spatial averages over different surface footprint dimensions. To facilitate the data processing the data are averaged onto regular grids so that corrected brightness temperatures can be assigned to each grid cell for all channels with footprint sizes appropriate to that cell.

Theoretical expressions for the antenna pattern effects have appeared many times in the literature and their application to earth-viewing microwave radiometers has been described by Claassen and Fung, Beck, and others [14], [15]. The application to the SMMR case has been described by Njoku [16]. A detailed description of the APC algorithm development and analysis for the SMMR is presented in [10] and only a brief summary will be given here.

The expression relating the brightness temperatures and antenna patterns to the antenna temperatures on a gridded array of data locations is given by

$$T_{Apj} = \frac{1}{\Lambda_p} \iint_{4\pi} \{G_{psj}T_{B\theta} + G_{ptj}T_{B\phi}\} \, d\Omega \qquad (2)$$

where $T_{B\theta}$ and $T_{B\phi}$ are the vertically and horizontally polarized brightness temperatures, respectively, G_{psj} and G_{ptj} are the vertical and horizontal co- or cross-polarized antenna patterns, Λ_p is a normalization factor, and T_{Apj} is the antenna temperature. The subscript p refers to polarization (either vertical v, or horizontal h), and the subscript j refers to averaged measurements corresponding to the jth grid cell in the SMMR swath. Equation (2) is a condensation of the more complete antenna temperature equation given in [10], in which can also be found a description of the gridding scheme. The essential purpose of the APC algorithm is to invert the form of (2), using antenna temperature measurements T_{Apj} and pre-computed antenna patterns G_{psj}, G_{ptj} to derive vertical and horizontal brightness temperatures $T_{B\theta}$, $T_{B\phi}$ for each grid cell. The evaluation of the integral in (2) over the solid angle region outside the earth's horizon is straightforward since space has a constant brightness temperature of 2.7 K. For the region within the earth horizon, but outside a central swath region, brightness temperature estimates are used to evaluate the contribution to the antenna temperature. Within the central swath region the remaining contribution to the integral of (2) is approximated in matrix form and the matrix is then inverted to derive brightness temperatures using the measured antenna temperatures themselves. Thus if T_{Apj}' is the antenna temperature for the jth cell with corrections for outside the central swath region, and Ω_m is the solid angle subtended by the mth cell, then

$$\overline{T}_A' = \overline{\overline{F}}\,\overline{T}_B \qquad \text{and} \quad \overline{T}_B = \overline{\overline{F}}^{-1}\overline{T}_A' \qquad (3)$$

where

$$F_{jm} = \frac{1}{\Lambda} \iint_{\Omega_m} G_j \, d\Omega.$$

(Subscript p, s, t notation has been suppressed here for simplicity.) An example of the output brightness temperatures is shown in the image of Fig. 16. For further details see [10].

V. INSTRUMENT PERFORMANCE SUMMARY

A. In-Flight Engineering Performance

The instrument operated continuously in orbit from July 6 until spacecraft failure on October 10, 1978, a period of 95 days. During this time interval the spacecraft encountered periods of occultation which produced instrument temperature variations with peak-to-peak values of up to 6 K with a mean of 300 K. On one occasion the motor casing for the antenna scan drive reached 319 K which represented the maximum temperature for any component in the instrument. The instrument was essentially thermally isolated from the other sensors on the spacecraft and was unaffected by their operation.

The temperature resolution ΔT remained significantly unchanged in orbit as referenced to the measured temperature resolutions taken during thermal-vacuum tests for the spacecraft and sensors at the integration facility one month prior to launch. Table III compares the temperature resolutions for the horizontal polarizations (and for the 37-GHz vertical channel) before launch and during October 1978—a week before the prime-power failure of the spacecraft.

Plots of the radiometer output voltage counts viewing cold space and the internal ambient reference loads for one complete orbit (rev 1255) are shown in Fig. 13. Conversion factors (voltage counts to degrees Kelvin) have been used to indicate the amount of variation in equivalent temperature units. The orbit begins at the equator at GMT 18:07:28. The ambient reference load responses shown in Fig. 13(a) indicate that throughout this particular orbit the ambient load mean radiometric data value remained stable to within 1.5 K for all channels. The cold sky radiometer responses are shown in Fig. 13(b). The anomaly appearing in all channels near the start of the orbit is due to the sun entering the sidelobes of the cold sky horns. Rev 1255 was one of the worst cases observed, in which the direction of the sun came within

TABLE III
SEASAT SMMR TEMPERATURE RESOLUTION SUMMARY

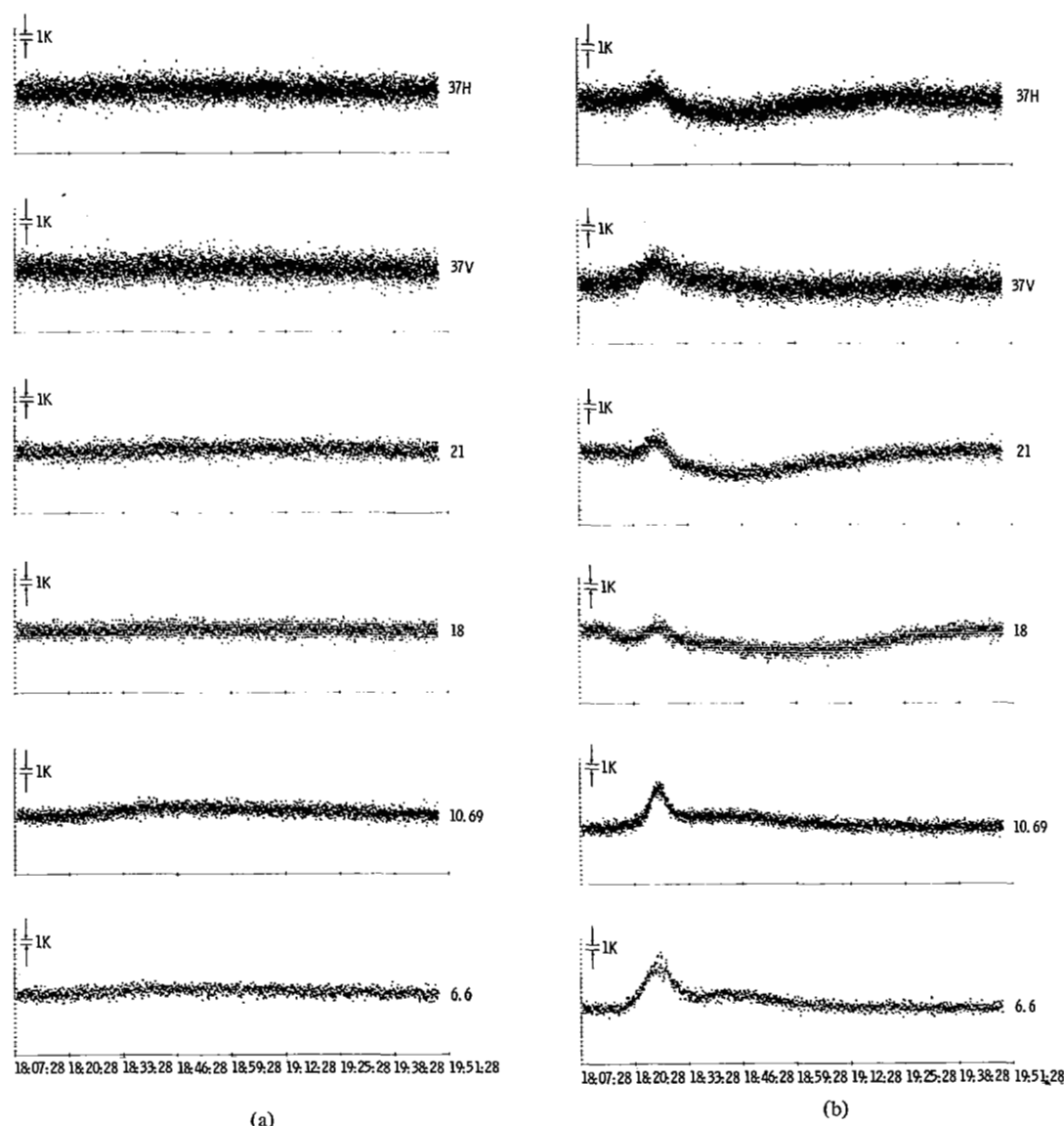| Freq. (GHz)	Thermal Vacuum May 1978		After 3-Months in Orbit October 1978	
	Temp. Resolution (K)	90% Conf. Limits (K)	Temp. Resolution (K)	90% Conf. Limits (K)
37H	1.35	(1.3-1.41)	1.44	(1.24-1.72)
37V	1.50	(1.44-1.57)	1.47	(1.27-1.76)
21	0.94	(0.88-1.0)	0.97	(0.84-1.16)
18	0.84	(0.79-0.88)	0.91	(0.78-1.09)
10.69	0.73	(0.69-0.78)	0.76	(0.66-0.91)
6.6	0.66	(0.61-0.72)	0.65	(0.56-0.78)

Fig. 13.   SMMR radiometric calibration data for rev 1255. (a) Ambient reference load. (b) Cold sky horn.

3° of the sky horn antenna beam axes. The resultant increases in measured brightness temperature are greatest at 6.6 GHz (about 10 K). Because of the sun's effects in the sky horns the sky measurements were not used in the calibration equations when increases of more than a few degrees Kelvin were observed.

In addition to the sun's effects, a number of other anomalies have been observed in the SMMR radiometric data. These occur mainly in the 6.6-GHz and 10.69-GHz channels and exhibit the characteristics of radio-frequency interference (RFI). While a thorough study of RFI effects in the SMMR data has not been performed, it appears that the visible effects
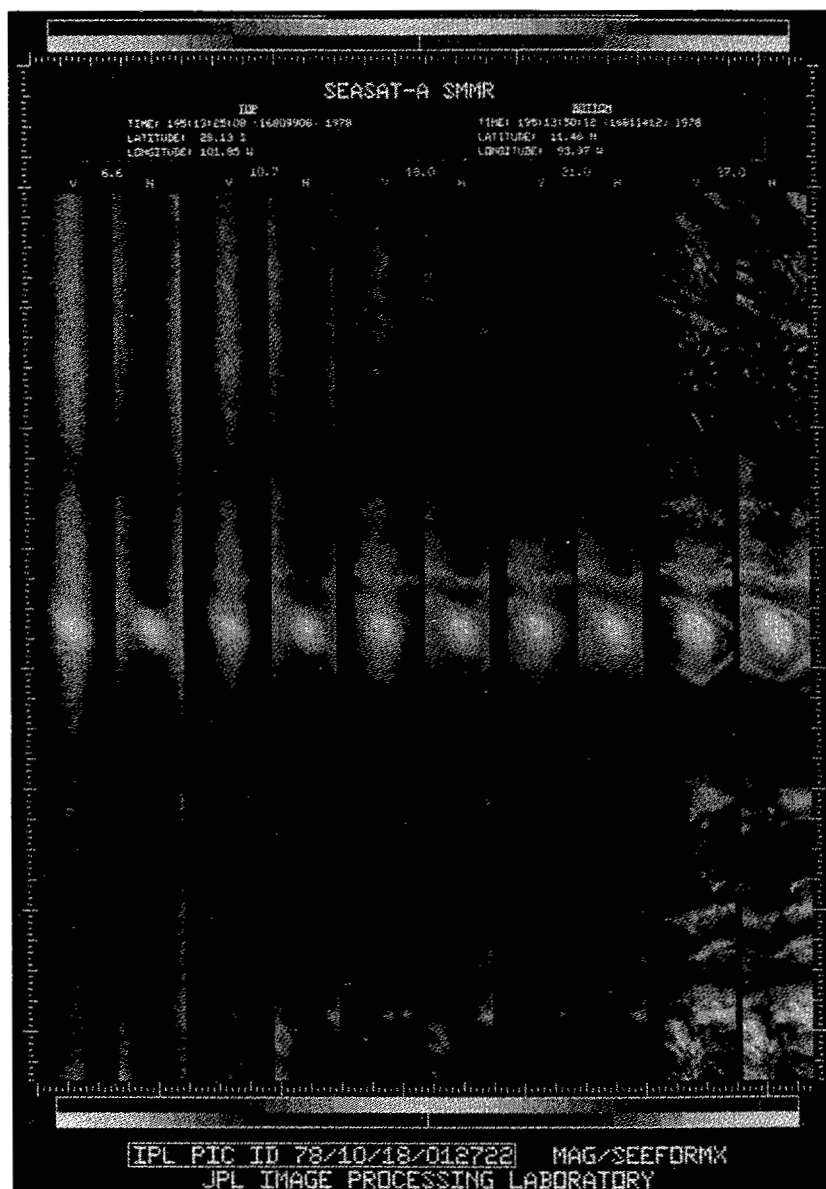
Fig. 14.   SMMR "raw data" image of Hurricane Fico, rev 251, July 14,
1978 (refer to text for details).

in the radiometric data are not widespread, and are restricted to highly urbanized land areas. However, it is possible that low levels of RFI may escape unnoticed and appear later as anomalies in the retrieved geophysical parameters.

B. Radiometric Data

The brightness temperatures are the calibrated and pattern-corrected instrument data products. The raw instrument data prior to calibration are in the form of digital voltages or "counts." These counts have been displayed in image format in Fig. 14 to illustrate the general features of the data at this level. The image shows a pass over Hurricane "Fico," July 14, 1978, with the hurricane centered at approximately 15.5°N, 123°W. The swath width of each vertical strip is approximately 595 km. The satellite was on an ascending pass, with time progressing from top to bottom of the image. Each strip corresponds to one channel of the SMMR, from 6.6-GHz

vertical polarization on the left to 37-GHz horizontal polarization on the right of the image. The gray scale is independently adjusted for each channel with a nonlinear Gaussian stretch between low brightness temperatures (dark) and high brightness temperatures (bright) (i.e., a histogram of each image intensity distribution fits a Gaussian). The best spatial resolution is available at 37 GHz where details of the cloud formations can be seen, and the structure of the hurricane is clearly visible including the "eye" region at the center. At 21 GHz a region of intermediate brightness extends for some distance away from the hurricane center corresponding to relatively high water vapor levels. At the lower frequencies there is less sensitivity to atmospheric effects and only the intense central region of the hurricane is visible. Two instrument effects are noticeable in the images. First, the offset sinusoidal scan pattern of the SMMR antenna has not been corrected for in the images; hence there is a geometrical distortion causing
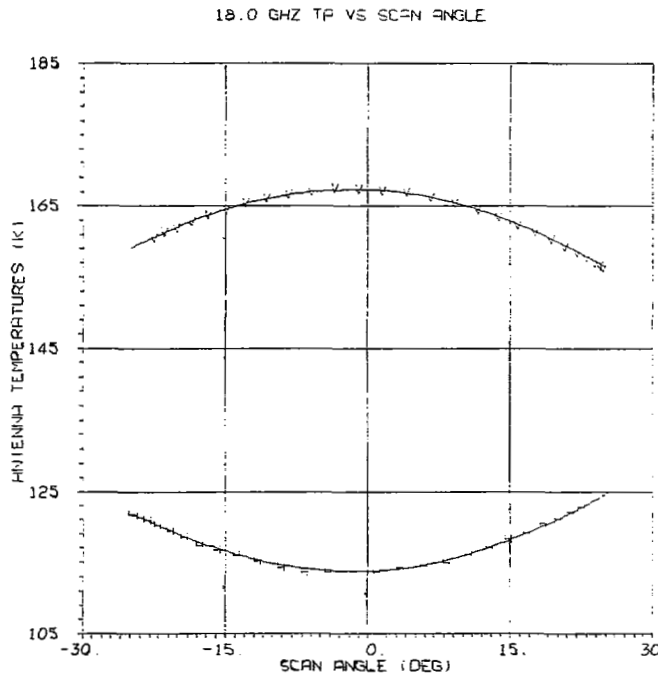
Fig. 15. Typical antenna temperature variation as a function of scan position caused by polarization cross coupling (18 GHz shown).

the hurricane to appear elliptical and slanted instead of circular. Secondly, the scanning of the reflector causes a rotation of the receiving polarizations, resulting in a coupling of orthogonally polarized radiation towards the scan extremes. This is most marked at 6.6 and 10.7 GHz for which there are significant differences between the vertically and horizontally polarized brightness temperatures. These antenna scan-induced effects are corrected for in the APC algorithms.

Fig. 15 shows the typical variation of antenna temperature as a function of scan angle. The data shown represent an average of several scans of SMMR data for which variations in scene brightness temperature across the scan have essentially been averaged out, and the residual variation in antenna temperature across the scan is due only to the antenna polarization coupling effects. The data points have been plotted for V (vertical polarization) and H (horizontal), using 18 GHz as a typical case. Curves have been drawn through the data points according to the theoretical expressions

$$T_{A_p} = T_{B\theta} G_{ps} + T_{B\phi} G_{pt} \qquad (4)$$

where

$$G_{ps} = g_{ps} \cos^2 \phi + g_{pt} \sin^2 \phi$$
$$+ (g_{ps} g_{pt})^{1/2} \sin 2\phi \cos \beta_p$$
$$G_{pt} = g_{pt} \cos^2 \phi + g_{ps} \sin^2 \phi$$
$$- (g_{ps} g_{pt})^{1/2} \sin 2\phi \cos \beta_p$$
$$p = v \text{ (vertical) or } h \text{ (horizontal)}.$$

Equation (4) is an approximate form of the complete antenna temperature equation given in [10] in which the brightness

temperature has been assumed constant across the scan, ϕ is the scan angle, and g_{pt}, g_{ps} are now integrated values. The curves have been fitted to the data in a least squares sense by adjusting the values of $\cos \beta_p$ [10]. The parameter $\cos \beta_p$ expresses the relative phase of the co- and cross-polarized antenna patterns. It is evident that nonzero values of $\cos \beta_p$ give rise to asymmetries in the antenna temperatures about the center scan position. Measurements of the antenna pattern relative phases were not made on the antenna range; thus their effect on the antenna temperature measurements is removed empirically in the APC algorithm. The magnitude of the polarization coupling at the ends of scan is clearly demonstrated by (4) and Fig. 15.

The brightness temperatures output from the instrument data processing algorithms are in a gridded format as produced by (3). To illustrate these data in brightness temperature units (Kelvins) a color image is shown in Fig. 16. In a manner similar to Fig. 14 the 10 SMMR channels have been displayed as strips from 6.6-GHz vertical on the left to 37-GHz horizontal on the right. Time progresses down the image; thus for this ascending pass north points downward. The image starts over central Africa at the top and progresses over the Mediterranean, France, England, Iceland, and Greenland. The image shows the brightness temperatures (color-coded according to the scale at the bottom) for a variety of surface types and phenomena. The humid tropical forest regions appear at the top with the Congo River visible in the higher spatial resolution channels, followed by regions of higher polarization contrasts across the sand deserts and plateaus of the Sahara. The Mediterranean Sea appears cold radiometrically with high polarization contrast, whereas the ocean north of England is masked somewhat at the higher frequencies by an extensive cloud feature extending toward Iceland. Less feature discrimination is possible at the spatial resolution of the 6.6- and 10.69-GHz frequencies whose primary applications are in large-area ocean parameter determinations. The periodic dark horizontal lines in the 10.7-GHz strips result from the image width (in pixels) not being a multiple of the number of data cells across the swath. The data blocks have been spaced apart to provide the same vertical dimension in the image as for the other channels.

Plots of antenna temperatures passing through Hurricane Fico on rev 331 are shown in Fig. 17 for some selected channels. Available surface-truth-derived winds at the time and location of the satellite overpass [17] have been used with surface and clear-atmosphere emission models [9] to calculate 10.69-GHz brightness temperatures; and, after removing a bias which includes antenna pattern effects, these have been plotted with the measured antenna temperatures in Fig. 17(b). They show that the relative dependence of the measured antenna temperatures on surface winds is in good agreement with the models, except for the central hurricane region where the additional effects of cloud and rain cause a sharp rise in the satellite data. In the geophysical processing stage these effects will be corrected for to extract the wind dependence alone.

A similar analysis has been performed for the sea-surface temperature dependence as shown in Fig. 18, where surface truth ocean temperatures have been used with an appropriate
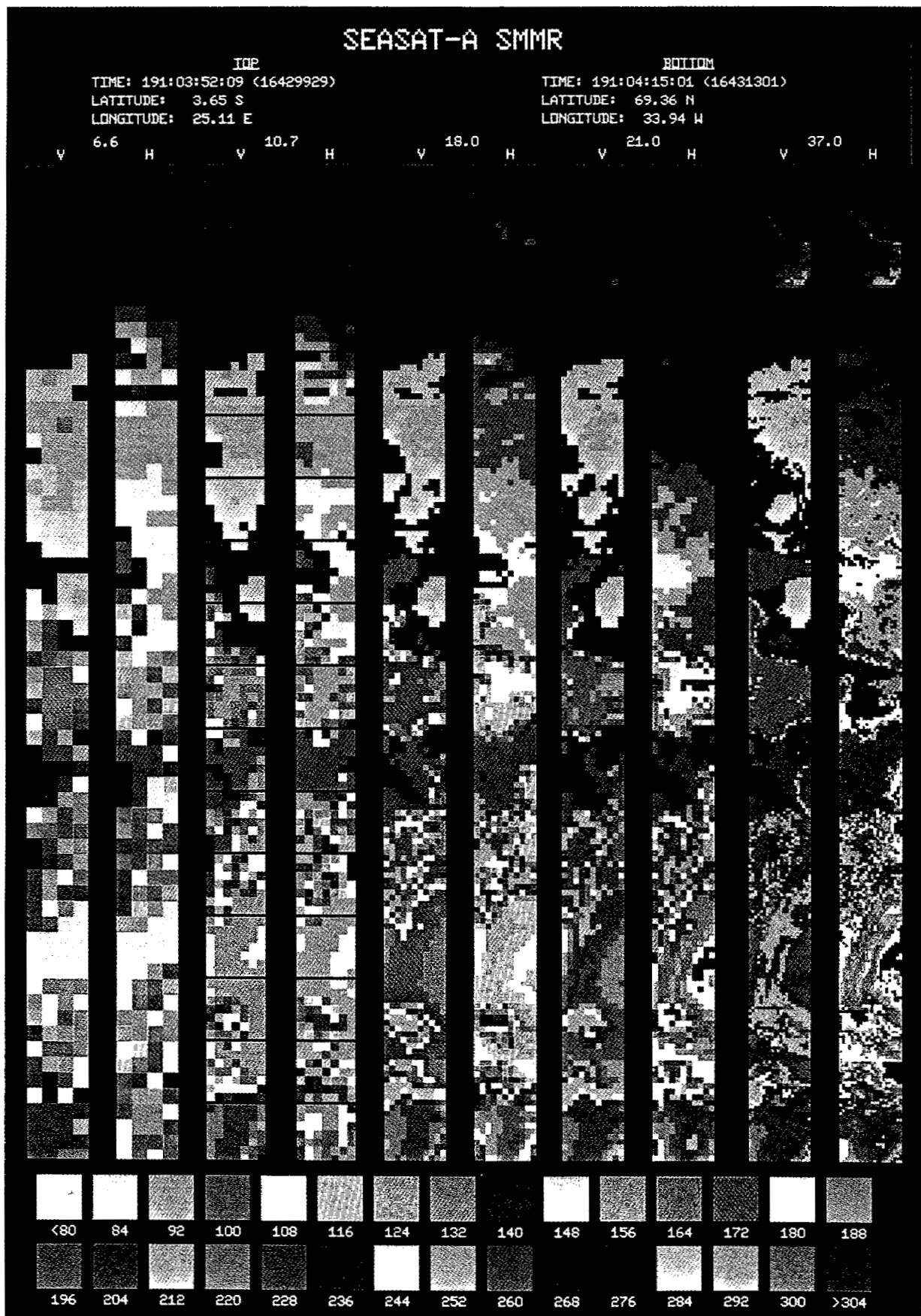
Fig. 16. SMMR color-coded brightness temperature image, rev 188, July 10, 1978. Image shows region from central Africa to Greenland.
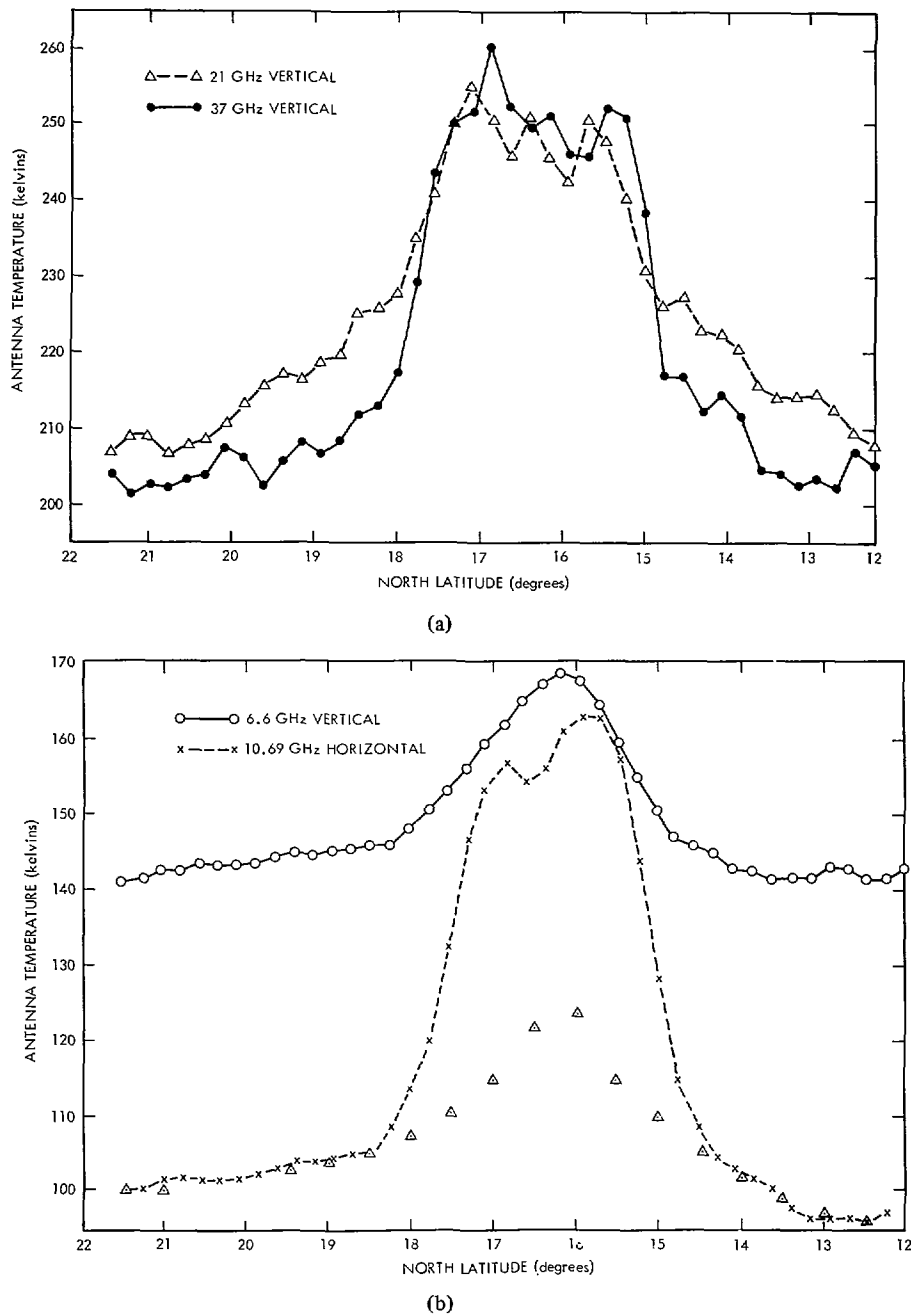
Fig. 17. SMMR antenna temperature data at the central scan position from a pass through Hurricane Fico (rev 331).
(a) 21 GHz and 37 GHz. (b) 6.6 GHz and 10.69 GHz. Theoretical antenna temperatures due to modeled wind-speed
dependence at 10.69 GHz are shown as triangles in (b).

emission model to compute antenna temperatures at 6.6 GHz to compare with the satellite data. The agreement is generally good except at the more northern latitudes where cloud and water vapor as evidenced by the 37- and 21-GHz data cause slight discrepancies. When these effects have been corrected for in the geophysical processing stage the accuracy to which sea-surface temperatures can be determined should approach the 1 to 1.5 K target. It is anticipated that an extended period of algorithm evaluation and surface truth comparisons will be required before the proof-of-concept objectives can

be satisfactorily demonstrated. Initial results of these geophysical evaluations are reported elsewhere [18].

VI. CONCLUSION

This paper has presented a description of the SMMR instrument, its modes of operation, the radiometer calibration procedures, and APC's. Analysis of the engineering and radiometric data has shown that over the 95-day Seasat lifetime the SMMR data acquired were of high quality. While complete geophysical processing of the data is still in progress at this
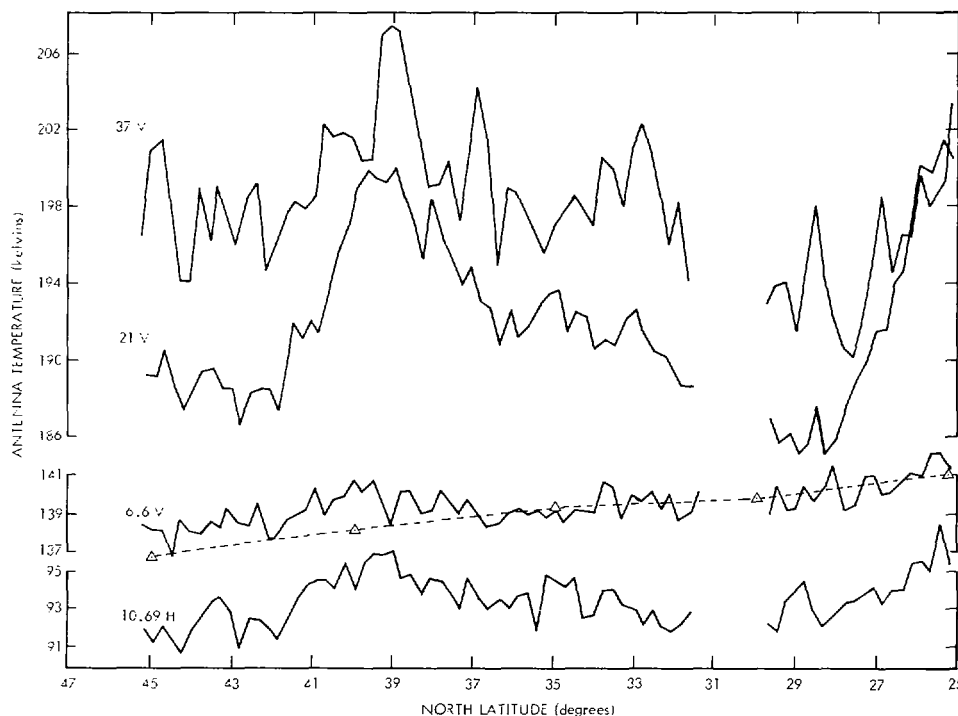
Fig. 18. SMMR antenna temperature data at the central scan position from a descending pass across the north Pacific Ocean (rev 331). Theoretical antenna temperatures due to modeled sea surface temperature dependence at 6.6 GHz are shown as triangles.

time, preliminary indications are that the major objectives in placing the SMMR in orbit should be achievable, auguring well for future applications of spacecraft microwave radiometry.

REFERENCES

[1] D. H. Staelin, "Passive remote sensing at microwave wavelengths," *Proc. IEEE*, vol. 57, Apr. 1969.

[2] W. Nordberg, J. Conaway, D. B. Ross, and T. Wilheit, "Measurements of microwave emission from a foam-covered, wind-driven sea," *J. Atmos. Sci.*, vol. 28, pp. 429–435, 1971.

[3] J. P. Hollinger, "Passive microwave measurements of sea-surface roughness," *IEEE Trans. Geosci. Electron.*, vol. GE-9, p. 169, 1971.

[4] D. H. Staelin, K. F. Kunzi, R. L. Pettyjohn, R. K. L. Poon, R. W. Wilcox, and J. W. Waters, "Remote sensing of atmospheric water vapor and liquid water with the Nimbus 5 microwave spectrometer," *J. Appl. Meteorol.* vol. 15, no. 11, 1976.

[5] K. F. Kunzi, A. D. Fisher, D. H. Staelin, and J. W. Waters, "Snow and ice surfaces measured by the Nimbus 5 microwave spectrometer," *J. Geophys. Res.*, vol. 81, no. 27, 1976.

[6] W. J. Campbell, P. Gloersen, W. J. Webster, T. T. Wilheit, and R. O. Ramseier, "Beaufort sea ice zones as delineated by microwave imagery," *J. Geophys. Res.*, vol. 81, pp. 1103–1110, 1976.

[7] T. T. Wilheit, A. T. C. Chang, M. S. V. Rao, E. B. Rodgers, and J. S. Theon, "A satellite technique for quantitatively mapping rainfall rates over the oceans," *J. Appl. Meteorol.* vol. 16, pp. 551–560, 1977.

[8] P. W. Rosenkranz, D. H. Staelin, and N. C. Grody, "Typhoon June (1975) viewed by a scanning microwave spectrometer," *J. Geophys. Res.*, vol. 83, pp. 1857–1868, 1978.

[9] T. T. Wilheit, "A review of applications of microwave radiometry to oceanography," *Boundary Layer Meteorol.*, vol. 13, pp. 277–293, 1978.

[10] E. G. Njoku, E. J. Christensen, and R. E. Cofield, "The Seasat scanning multichannel microwave radiometer (SMMR): Antenna pattern corrections—development and implementation," *IEEE J. Oceanic Eng.*, this issue pp. 125–137.

[11] P. N. Swanson and A. L. Riley, "The Seasat scanning multichannel microwave radiometer (SMMR): Radiometric calibration algorithm development and performance," *IEEE J. Oceanic Eng.*, this issue, pp. 116–124.

[12] P. Gloersen and F. T. Barath, "A scanning multichannel microwave radiometer for Nimbus-G and Seasat-A," *IEEE J. Oceanic Eng.*, vol. OE-2, Apr. 1977.

[13] A. W. Rudge and N. A. Adatia, "Offset-parabolic reflector antennas: A review," *Proc. IEEE*, vol. 66, Dec. 1978.

[14] J. P. Claassen and A. K. Fung, "The recovery of polarized apparent temperature distributions of flat scenes from antenna temperature measurements," *IEEE Trans. Antennas Propagat.*, vol. AP-22, pp. 433–442, 1974.

[15] F. B. Beck, "Antenna corrections to microwave radiometer temperature calculations," *Rad. Sci.*, vol. 10, pp. 839–845, 1975.

[16] E. G. Njoku, "Antenna pattern correction procedures for the scanning multichannel microwave radiometer (SMMR)," *Boundary Layer Meteorol.*, to be published, 1980.

[17] D. B. Ross, National Oceanic and Atmospheric Administration/AOML, Miami, FL, private communication, 1979.

[18] R. G. Lipes, R. L. Bernstein, V. J. Cardone, E. G. Njoku, A. L. Riley, D. B. Ross, C. T. Swift and F. J. Wentz, "Seasat scanning multichannel microwave radiometer: Results of the Gulf of Alaska workshop," *Science*, vol. 204, pp. 1415–1417, 1979.
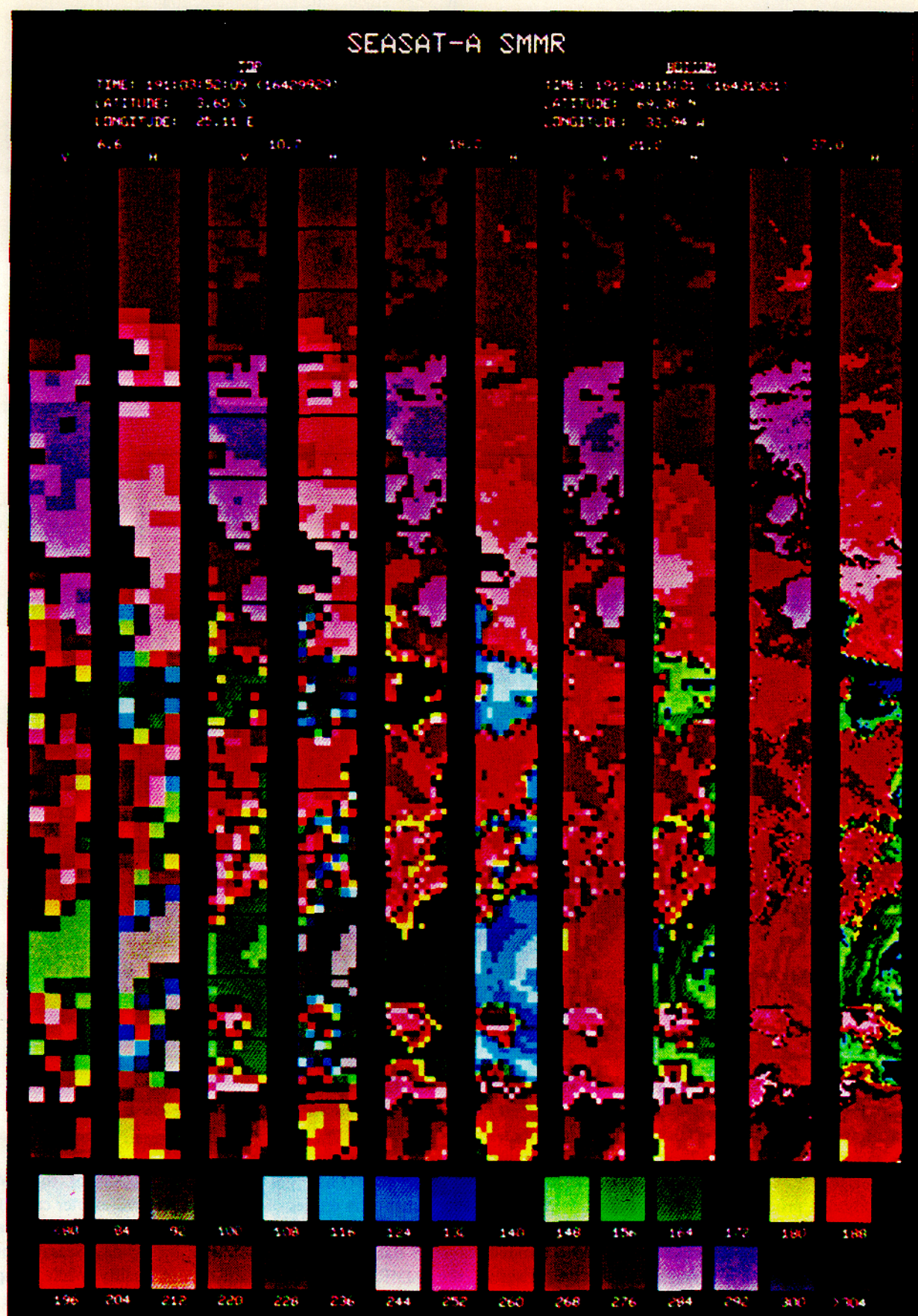
Fig. 16. SMMR color-coded brightness temperature image, rev 188, July 10, 1978. Image shows region from central Africa to Greenland